

# Differential Absorption Lidar to Measure Subhourly Variation of Tropospheric Ozone Profiles

Shi Kuang, John F. Burris, Michael J. Newchurch, Steve Johnson, and Stephanie Long

**Abstract**—A tropospheric ozone Differential Absorption Lidar system, developed jointly by The University of Alabama in Huntsville and the National Aeronautics and Space Administration, is making regular observations of ozone vertical distributions between 1 and 8 km with two receivers under both daytime and nighttime conditions using lasers at 285 and 291 nm. This paper describes the lidar system and analysis technique with some measurement examples. An iterative aerosol correction procedure reduces the retrieval error arising from differential aerosol backscatter in the lower troposphere. Lidar observations with coincident ozonesonde flights demonstrate that the retrieval accuracy ranges from better than 10% below 4 km to better than 20% below 8 km with 750-m vertical resolution and 10-min temporal integration.

**Index Terms**—Differential Absorption Lidar (DIAL), lidar, ozone, remote sensing, troposphere.

## I. INTRODUCTION

**O**ZONE IS A KEY trace-gas species within the troposphere. On the one hand, ozone is a precursor of the hydroxyl radical [1], which reacts with most trace species in the atmosphere. On the other hand, ozone is also a strong greenhouse gas influencing the climate by its radiative forcing [2]. *In situ* photochemistry and dynamic processes largely govern the distribution of tropospheric ozone [3]. Measuring ozone variability at high spatial and temporal resolution increases our understanding of tropospheric chemistry [4], [5], planetary boundary layer (PBL)–free-tropospheric exchange [6], [7], stratosphere–troposphere exchange [8]–[10], and the impact of lightning-generated  $\text{NO}_x$  on tropospheric ozone [11]–[14].

Several techniques currently exist for making range-resolved measurements of tropospheric ozone. The most common technique is the balloonborne electrochemical concentration cell,

which has monitored ozone since the 1960s. The ozonesonde profiles ozone with a 100-m vertical resolution from the surface to 35-km altitude with the accuracy of 5%–10% [15], [16]. Ozonesondes are attractive because of their low up-front cost and well-characterized behavior. However, they are not suitable for making continuous measurements because of logistical considerations. Interesting atmospheric phenomena that vary over periods less than one day are particularly difficult to monitor using balloon ozonesondes. Satellite observations can derive total column ozone [17] and stratospheric ozone [18]–[22] and extend measurements to altitudes that are inaccessible to ozonesondes. More recently, high-quality satellite observations of tropospheric ozone are becoming available [18], [23]–[33]. Although the satellite measurements can produce global maps of ozone, their current measurement uncertainties, along with their coarse spatial and temporal resolution, limit their ability to observe short-term variations in ozone. Lidars can supplement these techniques when a requirement exists for ozone retrievals with higher temporal (from 1 min to several hours) and vertical resolution (from tens of meters to 2 km). For example, lidars of the Network for the Detection of Atmospheric Composition Change [34], [35] are providing long-term observations of ozone, as well as aerosol, temperature, and water vapor. Although the up-front costs are considerably higher than for a balloon ozonesonde operation, lidars can acquire profiles continuously under both daytime and nighttime conditions. The spatial and temporal resolution of a lidar is more than sufficient to characterize short-term ozone variations for the photochemical studies of vertical processes.

Differential Absorption Lidar (DIAL) has been successfully used to measure ozone within the PBL [36], [37], the free troposphere [38]–[44], and the stratosphere [45]–[48] for several decades. DIAL is evolving from ground-based and airborne systems to systems that are suitable for long-term deployment in space [49]. The technique derives ozone concentrations by analyzing how rapidly the backscattered signals at two separate but closely spaced wavelengths, one strongly absorbed by ozone and the other less strongly absorbed, diminish with altitude. This measurement does not require knowledge of the absolute signal intensities but, rather, only the relative change of the two signals with respect to altitude. Using electronically gated detection permits range-resolved measurements to a resolution as small as several meters over acquisition times of several minutes. The ozone DIAL discussed in this paper is located in the southeastern U.S. and thus provides a unique observational site within an interesting scientific area [50] to study trace-gas transport at the midlatitudes for both the polluted PBL and the free troposphere.

Manuscript received July 31, 2009; revised March 9, 2010. This work was supported in part by the National Aeronautics and Space Administration (NASA)'s Science Mission Directorate and in part by the National Oceanic and Atmospheric Administration's National Environmental Satellite, Data, and Information Service.

S. Kuang and M. J. Newchurch are with the Atmospheric Science Department, The University of Alabama in Huntsville (UAHuntsville), Huntsville, AL 35805 USA (e-mail: mike@nsstc.uah.edu).

J. F. Burris is with the Goddard Space Flight Center, NASA, Greenbelt, MD 20771 USA.

S. Johnson is with the Marshall Space Flight Center, NASA, Huntsville, AL 35812 USA.

S. Long is with the Department of Physics, UAHuntsville, Huntsville, AL 35899 USA.

Color versions of one or more of the figures in this paper are available online at <http://ieeexplore.ieee.org>.

Digital Object Identifier 10.1109/TGRS.2010.2054834

84

## II. SYSTEM DESCRIPTION

85 Housed in the Regional Atmospheric Profiling Center for  
 86 Discovery (RAPCD), the tropospheric ozone DIAL system is  
 87 located at 34.7250° N, 86.6450° W on the campus of The  
 88 University of Alabama in Huntsville (UAHuntsville) within  
 89 the Huntsville city limits at an elevation of 206 m above  
 90 sea level. It is designed for measurements within the PBL  
 91 and the free troposphere during both daytime and nighttime.  
 92 Because of UAHuntsville's location and occasional high tem-  
 93 perature and humidity conditions, heavy aerosol pollution is  
 94 sometimes present. Compared with the clean free troposphere,  
 95 these aerosols require a larger dynamic range for the detection  
 96 system because of their larger optical depth. Moreover, the  
 97 rapid change of aerosol concentrations (e.g., due to convec-  
 98 tive activity) increases the measurement uncertainty for DIAL  
 99 within the PBL and lower troposphere. Judicious system-design  
 100 choices and an effective aerosol correction scheme allow this  
 101 system to produce high-quality ozone profiles under a variety  
 102 of conditions.

### 103 A. Wavelength Selection

104 The selection of the 285- and 291-nm wavelengths re-  
 105 sults from the balance of the following three considerations:  
 106 1) optimizing the altitude range to make retrievals; 2) reducing  
 107 the impact of the solar background during daytime operation;  
 108 and 3) reducing the impact of aerosol interference upon the  
 109 ozone retrieval. The DIAL wavelength selection is flexible  
 110 and optimized for the local ozone distribution, the absorption  
 111 arising from non-ozone species, the measurement range, and  
 112 the specific system configuration, including the output power,  
 113 the telescope mirror size, and the photomultiplier's (PMT's)  
 114 dynamic range. Numerous publications (e.g., [51]) discussed  
 115 the optimum wavelengths for tropospheric systems. Although  
 116 shorter wavelengths can provide higher measurement sensitiv-  
 117 ity arising from the larger ozone differential cross section, they  
 118 limit the maximum measurable range due to stronger attenua-  
 119 tion of ozone absorption and Rayleigh (molecular) extinction  
 120 and thus require more signal acquisition time. In addition,  
 121 the shorter wavelengths require more dynamic range of the  
 122 detection system and might require more altitude channels.  
 123 With the current transmitter power, the online wavelength of  
 124 285 nm allows us to measure ozone up to 9 km under a clear  
 125 sky and 7 km under aerosol loading with a 10-min temporal  
 126 resolution. Because of the significant solar background during  
 127 daytime operations, we choose 291 nm as the offline wave-  
 128 length. Longer wavelengths will cause a significant increase  
 129 in the solar background and reduce the signal-to-background  
 130 ratio. To measure both wavelength channels using the same  
 131 PMT and simplify the system design, we used a bandpass filter  
 132 with a central wavelength of 286.4 nm and a full width at half  
 133 maximum of 11 nm whose transmittance is  $\leq 10^{-8}$  at wave-  
 134 lengths longer than 300 nm. For a bandpass filter, the integrated  
 135 sky background over the filter bandwidth and the dark counts  
 136 actually determine the background for both offline and online  
 137 wavelengths. For our lidar configuration, the 285- and 291-nm  
 138 wavelength region can provide sufficient signal-to-background

ratios at 8 km under most sky conditions. The retrieval errors  
 139 due to aerosol interference are a concern in the PBL and  
 140 lower troposphere. These errors are not a simple function of  
 141 the wavelength separations because reducing the separation to  
 142 reduce the aerosol differential backscattering will also decrease  
 143 the differential ozone cross section. These errors are sensitive  
 144 to the local aerosol composition, size distribution, and vertical  
 145 profile. Although the aerosol interference can be lower when  
 146 our online wavelength extends to the steepest part of the ozone  
 147 absorption cross section, this will significantly sacrifice the  
 148 maximum measurable range. Therefore, the 285–291-nm pair  
 149 is the optimal choice to balance the maximum measurable  
 150 altitude, the impact of aerosol differential backscattering, and  
 151 the impact of solar background. 152

### B. Hardware Components

153

Table I lists the characteristics of the RAPCD ozone DIAL  
 154 system. The transmitter consists of two identical dye lasers  
 155 pumped by two separate frequency-doubled Nd:YAG lasers  
 156 (Fig. 1). A pulse generator triggers each laser pulse with a  
 157 25-ms separation between the alternate pulses. The dye lasers  
 158 are software controlled to select the user-defined wavelength.  
 159 The knife-edge method [52] determines that the divergences  
 160 of both UV laser beams are less than 1 mrad. A 0.75-m  
 161 triple-grating monochromator (Acton Research Corporation)  
 162 indicates that the actual wavelengths of the outgoing UV lasers  
 163 are 285 and 291 nm within an uncertainty of 0.1 nm. 164

The receiving system currently operates with two separate  
 165 telescopes, as shown in Fig. 2. The high-altitude receiver uses  
 166 a 40-cm Newtonian telescope, and the low-altitude channel  
 167 employs a 10-cm Cassegrain telescope. The large telescope  
 168 system routinely makes measurements from 3 to 8 km and,  
 169 on occasion, measures ozone at 12 km. Employing a 1.5-mrad  
 170 field of view (FOV), the large telescope achieves full overlap  
 171 between the laser and receiver at about 3 km. Larger FOVs  
 172 lower the altitude at which full overlap occurs but significantly  
 173 increase solar background. The small telescope system cur-  
 174 rently retrieves ozone between 1 and about 5 km with a typical  
 175 FOV of 4.3 mrad. The future plan is to extend the retrievals  
 176 down to about 200 m with an additional altitude channel in the  
 177 small telescope. The bandpass filters used to restrict the solar  
 178 background for both receivers have a transmittance of 35% at  
 179 285 nm and 20% at 291 nm. 180

The detection system of the RAPCD ozone DIAL uses both  
 181 photon counting (PC) and analog detection to facilitate oper-  
 182 ations over both altitude channels. This detection combination  
 183 provides the linearity of the analog signal in the strong-signal  
 184 region and high sensitivity of the PC signal in the weak-signal  
 185 region. An EMI 9813 QA PMT, which has been used exten-  
 186 sively for many years on a number of Goddard Space Flight  
 187 Center lidar systems [53], [54], is used in the high-altitude  
 188 channel, while a small Hamamatsu 7400 PMT is used in the  
 189 low-altitude channel. A photodiode detects the outgoing laser  
 190 pulses, which trigger both the PMT gating circuits and the Licel  
 191 transient recorder (TR) (TR40-80, Licel Company, Germany).  
 192 The Licel TR offers the advantage of increased dynamic range  
 193 by providing simultaneous measurements using both analog 194

TABLE I  
 CHARACTERISTICS OF THE RAPCD OZONE DIAL SYSTEM

System	Specification	
<b>Transmitter</b>		
Pump lasers	Nd:YAG, 20 Hz repetition rate, 5-7 ns pulse length, 300 mJ pulse <sup>-1</sup> at 1064 nm, 50 mJ pulse <sup>-1</sup> at 532 nm	
Dye	Rhodamine 590 and 610	
Emitted UV	4 mJ pulse <sup>-1</sup> at 285 nm, divergence <1 mrad 3 mJ pulse <sup>-1</sup> at 291 nm, divergence <1 mrad	
Tuning range	277 to 303 nm for the final UV output	
<b>Receiver</b>		
	High-altitude channel	Low-altitude channel
Telescope	Newtonian, 40-cm diameter, f/4.5, 1.5-mrad FOV	Welch Mechanical Designs Cassegrain, 10-cm diameter, f/2.3, 4.3-mrad FOV
Band-pass filter	Center wavelength at 286.4 nm with a 11-nm FWHM. Transmittance is 35% at 285 nm and 20% at 291 nm	
Detector	Electron Tubes 9813QA, about 28% quantum efficiency	Hamamatsu R7400U-03, about 20% quantum efficiency
Signal processing	LICEL Transient Recorder (TR40-80), 250-MHz maximum photoncounting rate, 12-bit and 40-MHz analog-to-digital converter, 25-ns range resolution	

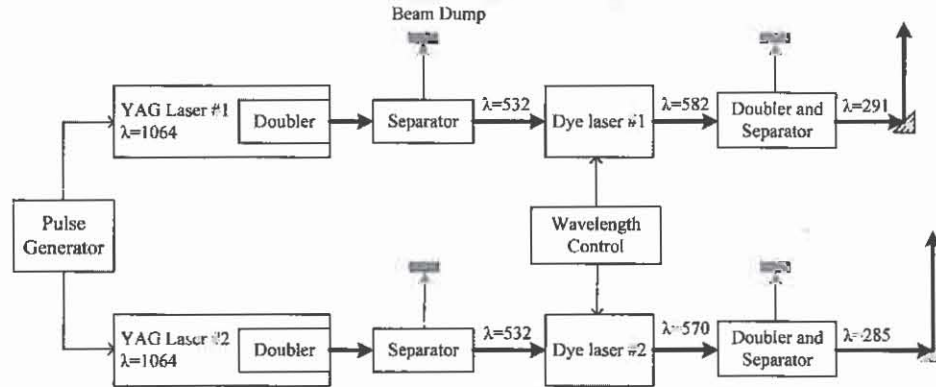


Fig. 1. Transmitter diagram.

195 detection and PC. The Licel TR's highest temporal resolution  
 196 is 25 ns, corresponding to a fundamental range resolution of  
 197 3.75 m. It is necessary to gate the high-altitude channel off  
 198 for the first 10–15  $\mu$ s and the low-altitude channel for the first  
 199 1  $\mu$ s to maintain the PMT's linearity and minimize the impact  
 200 of signal-induced bias (SIB) on the background count rate.

### 201 III. DATA PROCESSING

#### 202 A. Raw Data Processing

203 Several operations, designed to improve the measurement  
 204 precision, occur before the ozone retrieval. First, average the  
 205 signal returns over 10 min and 150 m. The temporal resolution  
 206 of the retrieval can be varied depending on the signal-to-noise  
 207 ratio (SNR). Second, apply a dead-time correction to the PC

signals. For PC at high counting rates, a second pulse arriving  
 208 at the discriminator before it has recovered from the previous  
 209 pulse will not be counted—a period known as dead time [55].  
 210 Experiments with a function-generator-driven LED determine  
 211 this time to be 10 ns for the high-altitude channel and 4 ns  
 212 for the low-altitude channel. Our results show that the system  
 213 dead time obeys a nonparalyzable model following a simple  
 214 relationship, as in (1)[56], between the true count rate  $C_T$  and  
 215 measured count rates  $C_M$ , allowing the impact of dead time  $T_d$   
 216 on the data to be removed  
 217

$$C_T = \frac{C_M}{1 - C_M T_d} \quad (1)$$

Third, remove the signal background. The last 10  $\mu$ s (400  
 218 fundamental bins) of signals ranging up to 30.72 km (far-range  
 219

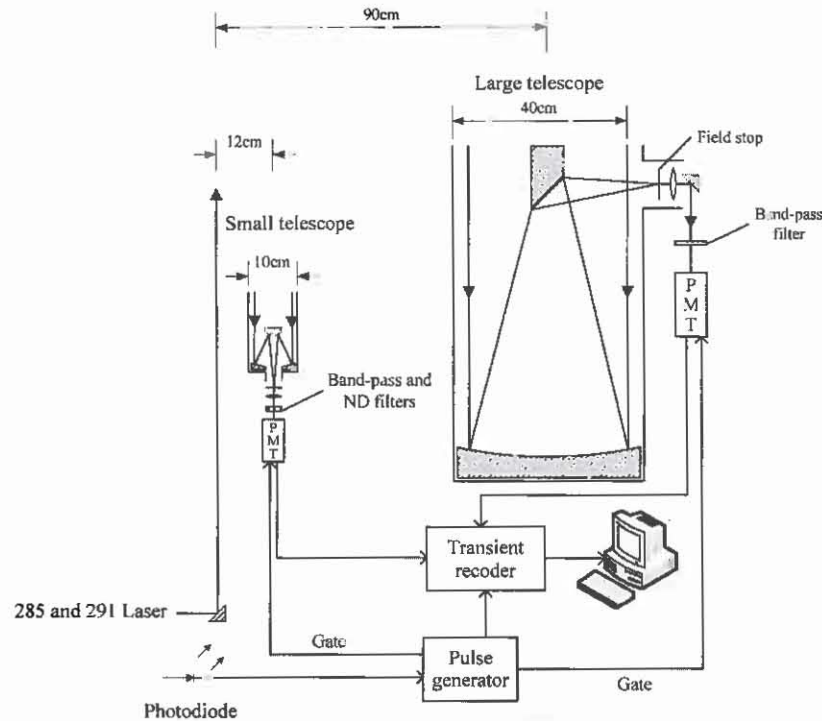


Fig. 2. Diagram of the receivers and detectors.

220 limit), which are considered to be the background region where  
 221 no laser signal returns are expected, are averaged to give an  
 222 approximate background. Fourth, merge the parallel analog and  
 223 PC signals into a single profile [57] after removing the offset  
 224 between the analog and PC signals [58]. We found this offset to  
 225 be about 250 ns for our system by carefully comparing returns  
 226 derived with clouds on both the analog and PC channels. The  
 227 merged region requires that the ratio of PC to analog signals is  
 228 constant. Ratios that are not constant suggest either an incorrect  
 229 background subtraction or a wrong dead-time correction. The  
 230 merging threshold of the PC signal is typically 20 MHz for  
 231 the Hamamatsu PMT employed in our low-altitude channel  
 232 and 20–30 MHz for the EMI PMT used on the high-altitude  
 233 channel. Because DIAL retrievals depend on the quality of  
 234 both 285- and 291-nm signals, we combine the PC and analog  
 235 signals approximately at the same altitude for both lasers to  
 236 minimize the retrieval error due to the merging. Examples of  
 237 the ratio of PC to analog signals and their merged region for  
 238 the 285-nm signal are shown in Fig. 3. The merging threshold  
 239 is 20 MHz for both altitude channels. The fifth step involves  
 240 smoothing the signals to reduce random noise. Our configura-  
 241 tion currently employs a five-point ( $5 \times 150 = 750$  m) running  
 242 average applied to returns from all altitudes; smoothing reduces  
 243 the effective vertical resolution to 750 m.

244 After initial processing, an exponential-fit correction re-  
 245 moves SIB from the signal returns. This bias, caused by intense  
 246 light returns from the near range (also called signal-induced  
 247 noise), appears as a slowly decaying noise source superimposed  
 248 on the normal returns. The causes of the SIB are related to the  
 249 regenerative effects such as dynode glow, after-pulsing effect,  
 250 glass-charging effect, shielding effect, and helium penetration  
 251 [59]. SIB varies widely with different PMTs. For our case, the

SIB of the EMI 9813 is larger than that for the Hamamatsu 252  
 7400. SIB can persist for several hundreds of microseconds and 253  
 can exert a strong influence on data at the lidar's upper range 254  
 where both signal and noise counts become comparable. With 255  
 uncorrected SIB, the raw signal falls off more slowly at higher 256  
 altitudes, resulting in lower retrieved ozone values. SIB usually 257  
 has more influence on the shorter wavelength channel, which 258  
 falls off more rapidly with altitude. Unless a mechanical shutter 259  
 physically blocks the optical path to the PMT to eliminate SIB, 260  
 a model must characterize its behavior. Cairo *et al.* [60] and 261  
 Zhao [61] have successfully used a double-exponential function 262  
 for this purpose. However, this correction increases measure- 263  
 ment uncertainties because both the scaling and exponential 264  
 lifetimes are difficult to determine without additional indepen- 265  
 dent measurements. A more practical technique is to employ 266  
 a single-exponential fit to the residual background [42], [43], 267  
 [62]. For the high-altitude channel, the function's coefficients 268  
 are automatically determined using a single-exponential least 269  
 squares fit to data acquired approximately from 100 to 160  $\mu$ s 270  
 after data acquisition starts where the SIB becomes dominant. 271  
 The start and length of the exponential fit vary with different 272  
 channels (either wavelength channels or altitude channels), 273  
 atmospheric structures, and lidar configurations because these 274  
 parameters affect the intensity of the detected signal. For our 275  
 low-altitude channel, the SIB is weaker than that of the high- 276  
 altitude channel because of the different PMT and weaker 277  
 signal. However, it is difficult to automatically determine the 278  
 fitting function for the low-altitude channel signal using the 279  
 least squares fitting method, particularly for the 285-nm sig- 280  
 nal, because the far-range signal after background correction 281  
 is not completely characterized by an exponential function 282  
 [Fig. 3(b)]. It is useful to optimize the exponential fitting 283

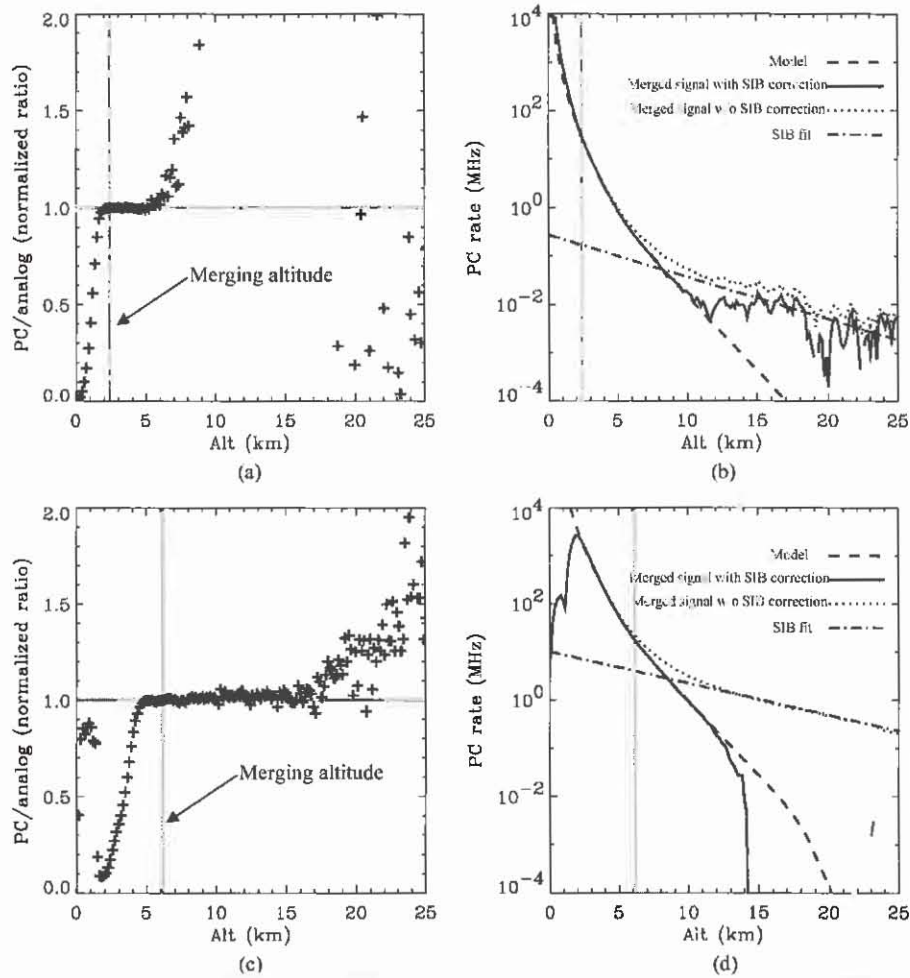


Fig. 3. Examples of signal merging and SIB correction for the 285-nm signal. The 10-min averaged data occurred at 13:00 local time on October 18, 2008. (a) Normalized ratio of PC to analog after background and dead-time corrections for the low-altitude channel signal. (b) Comparison of the non-SIB-corrected signal, the SIB-corrected signal, and the model, as well as the SIB fitting function, for the low-altitude signal. The model uses the coincident ozonesonde measurement assuming no aerosol. The SIB fitting function ( $\exp(-1.3 - \alpha/t \cdot 2 \cdot 10^{-1})$ ) was empirically derived using previously retrieved data and coincident ozonesonde measurements. (c) Same as (a) but for the high-altitude channel. (d) Same as (b) but for the high-altitude channel. The coefficients of the SIB fitting function result from an empirical single-exponential least squares fit to the signal acquired from 100 to 160  $\mu$ s after data acquisition starts.

284 function for the low-altitude channel using previous retrieval  
 285 data and compare the data with coincident ozonesonde profiles.  
 286 The slope of the logarithm of the SIB fitting function remains  
 287 for a particular configuration (i.e., outgoing power) and could  
 288 slightly change for different configurations. Those retrievals  
 289 corrected using the empirically derived exponential function  
 290 agree with ozonesonde profiles up to 5 km within 5% bias.  
 291 Fig. 3 shows the typical effect of the SIB correction and the  
 292 comparison of the fully corrected signal and the model for the  
 293 285-nm signal. The model simulation employs the coincident  
 294 ozonesonde measurement assuming no aerosol.

### 295 B. DIAL Retrieval

296 Excellent discussions concerning the DIAL technique occur  
 297 in the publications by Measures [63], Kovalev and Eichinger  
 298 [64], and Browell *et al.* [39]. The average ozone number density  
 299  $n_{(r+\Delta r/2)}$  between range  $r$  and  $r + \Delta r$  can be expressed as  
 300 the summation of the signal term  $n_{(r+\Delta r/2)}^s$ , the differential

backscattering term  $\Delta n_{(r+\Delta r/2)}^b$ , and the differential extinction  
 term  $\Delta n_{(r+\Delta r/2)}^e$  301 302

$$n_{(r+\Delta r/2)} = n_{(r+\Delta r/2)}^s + \Delta n_{(r+\Delta r/2)}^b + \Delta n_{(r+\Delta r/2)}^e. \quad (2)$$

One can write the discrete forms of the three terms at the right  
 side as follows: 303 304

$$n_{(r+\Delta r/2)}^s = \frac{1}{2\Delta r \Delta \sigma_{O_3}} \ln \left( \frac{P_{on}(r) P_{off}(r+\Delta r)}{P_{off}(r) P_{on}(r+\Delta r)} \right) \quad (3)$$

$$\Delta n_{(r+\Delta r/2)}^b = - \frac{1}{2\Delta r \Delta \sigma_{O_3}} \ln \left( \frac{\beta_{on}(r) \beta_{off}(r+\Delta r)}{\beta_{off}(r) \beta_{on}(r+\Delta r)} \right) \quad (4)$$

$$\Delta n_{(r+\Delta r/2)}^e = - \frac{1}{\Delta \sigma_{O_3}} (\alpha_{on}(r+\Delta r/2) - \alpha_{off}(r+\Delta r/2)) \quad (5)$$

where the subscripts “on” and “off” represent the online  
 (285 nm) and offline (291 nm) wavelengths, respectively,  $P$  is  
 the detected photon counts,  $\beta$  is the total backscatter coefficient, 305 307

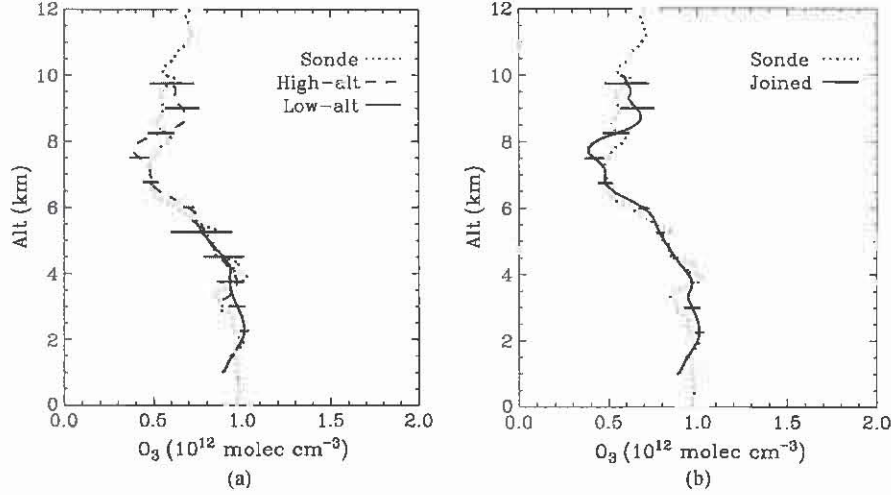


Fig. 4. Example of a joined ozone retrieval for the lidar data in Fig. 3. (a) Separate retrievals of the two altitude channels. The error bars represent the one-sigma statistical uncertainties. The gray envelope represents  $\pm 10\%$  uncertainty of the coincident ozonesonde profile. (b) Joined DIAL retrieval from the two altitude channels and its combined one-sigma statistical uncertainty.

308  $\alpha$  is the total extinction coefficient excluding ozone, and  $\Delta\sigma_{O_3}$   
 309 is the differential ozone absorption cross section.  $P$ ,  $\beta$ , and  
 310  $\alpha$  are dependent on  $r$  and the wavelength. Strictly speaking,  
 311  $\Delta\sigma_{O_3}$  is  $r$  dependent as well because it is a function of tempera-  
 312 ture, which varies with  $r$ . By ignoring the differential scattering  
 313 and extinction from non-ozone species, the DIAL equation re-  
 314 duces to only  $n^s$ .  $\Delta n^b$  arises from aerosol differential backscat-  
 315 tering.  $\Delta n^c$  consists of differential Rayleigh extinction, aerosol  
 316 extinction, and non-ozone gaseous absorption, including  $O_2$ ,  
 317  $SO_2$ , and  $NO_2$ . Measurements from a meteorological sounding  
 318 can usually correct Rayleigh effects. We correct the aerosol  
 319 effects when they are significantly enough, particularly in PBL.  
 320 The aerosol correction discussion appears in Section III-D.

### 321 C. Joining Retrievals From Two Adjacent Altitude Channels

322 Final retrievals result from joining the data from two altitude  
 323 channels with a weighted average. We choose to join the final  
 324 ozone retrievals instead of the raw signals because the SNRs of  
 325 the two altitude channels at the joining altitude are significantly  
 326 different. If the retrievals derived from two different channels  
 327 are statistically independent, the best estimate of these measure-  
 328 ments is the two-channel weighted average [65]

$$n_{\text{best}} = \frac{\sum_{i=1}^2 w_i n_i}{\sum_{i=1}^2 w_i} \quad (6)$$

329 where  $n_i$  is the ozone retrieval of channel  $i$  and the weight  $w_i$   
 330 is the inverse square of the corresponding statistical uncertainty  
 331 ( $\varepsilon_{1i}$ , which will be discussed in Section V)

$$w_i = 1/\varepsilon_{1i}^2. \quad (7)$$

332 The uncertainty of  $n_{\text{best}}$  is

$$\varepsilon_{1\text{best}} = \left( \sum_{i=1}^2 w_i \right)^{-1/2} \quad (8)$$

Typically, the low- and high-altitude channels join between 333  
 3.3 and 4.4 km. Fig 4 shows an example of a joined ozone 334  
 profile, as well as the combined one-sigma statistical uncer- 335  
 tainties. 336

### D. Aerosol Correction

In a polluted area, aerosols can be a dominant error source 338  
 in the lower troposphere. Based on (4) and (5), the vertical 339  
 gradient of aerosol backscattering determines  $\Delta n^b$ , and the 340  
 magnitude of the differential aerosol extinction coefficient de- 341  
 termines  $\Delta n^e$ . The largest aerosol correction usually occurs in 342  
 an inhomogeneous aerosol layer (i.e., the top of the PBL). One 343  
 can solve for the ozone and aerosol profiles simultaneously with 344  
 only two wavelengths by assuming appropriate Ångström expo- 345  
 nents and constant lidar ratios [66], [67]. If a third wavelength 346  
 is available and is close to the DIAL wavelength pair, one can 347  
 use the dual-DIAL technique [68], [69] to reduce the error due 348  
 to aerosol. When the third wavelength is far from the DIAL 349  
 wavelength pair, one can use the method suggested by Browell 350  
*et al.* [39] to correct the aerosol interference. Without the third 351  
 wavelength, we employ an iterative procedure to retrieve ozone 352  
 and correct aerosol effects. To illustrate this method, start with 353  
 the equation for ozone number density using only the 291-nm 354  
 signal [63] 355

$$\begin{aligned} & n_{(r+\Delta r/2)} \\ &= \frac{1}{2\sigma_{O_3}\Delta r} \\ & \times \left\{ \ln \left( \frac{P(r)}{P(r+\Delta r)} \right) - \ln \left[ \frac{(\beta_{(r)}^M + \beta_{(r)}^A)/r^2}{(\beta_{(r+\Delta r)}^M + \beta_{(r+\Delta r)}^A)/(r+\Delta r)^2} \right] \right. \\ & \left. - 2 \left( \alpha_{(r+\Delta r/2)}^M + \alpha_{(r+\Delta r/2)}^A \right) \Delta r \right\} \quad (9) \end{aligned}$$

356 where  $\sigma_{O_3}$  is the ozone absorption cross section,  $\beta_{(r)}^M$  and  
 357  $\beta_{(r)}^A$  are the molecular and aerosol backscatter coefficients at  
 358 range  $r$ , respectively, and  $\alpha_{(r+\Delta r/2)}^M$  and  $\alpha_{(r+\Delta r/2)}^A$  represent  
 359 the average molecular and aerosol extinction coefficients, re-  
 360 spectively, between range  $r$  and  $r + \Delta r$ . The subscript 291  
 361 is omitted for brevity because all backscatter and extinction  
 362 parameters correspond to 291 nm. Solving for  $\beta_{(r)}^A$ , (9) becomes

$$\beta_{(r)}^A = \exp \left\{ \ln \left( \frac{P(r)}{P(r+\Delta r)} \right) - 2n_{(r+\Delta r/2)} \sigma_{O_3} \Delta r \right. \\ \left. - 2 \left( \alpha_{(r+\Delta r/2)}^M + \alpha_{(r+\Delta r/2)}^A \right) \Delta r \right\} \\ \times \frac{r^2 \left( \beta_{(r+\Delta r)}^M + \beta_{(r+\Delta r)}^A \right)}{(r + \Delta r)^2} = \beta_{(r)}^M. \quad (10)$$

363 Assuming that the lidar ratio (aerosol extinction-to-backscatter  
 364 ratio), i.e.,  $S = \alpha^A / \beta^A$ , is known for the 291-nm signal and  
 365 further assuming that

$$\alpha_{(r+\Delta r/2)}^A \approx \alpha_{(r+\Delta r)}^A = S \beta_{(r+\Delta r)}^A \quad (11)$$

366 (10) only contains the following two unknown variables: the  
 367 aerosol backscatter coefficient  $\beta_{(r+\Delta r)}^A$  and the ozone number  
 368 density  $n_{(r+\Delta r/2)}$ . Molecular backscatter and extinction can be  
 369 computed from nearby radiosonde data or from climatology.  
 370 For the first iteration step,  $n_{(r+\Delta r/2)}$  can be computed from  
 371 (3) and inserted into (10). By assuming a start value  $\beta_{(ref)}^A$  at a  
 372 reference range and a constant  $S$  with range,  $\beta_{(r)}^A$  can be solved  
 373 by (10). Then, the first  $\beta_{(r)}^A$  profile is substituted back into (10)  
 374 to compute the second estimate by using a more accurate form  
 375 for  $\alpha_{(r+\Delta r/2)}^A$  as

$$\alpha_{(r+\Delta r/2)}^A = S \left( \beta_{(r+\Delta r)}^A + \beta_{(r)}^A \right) / 2 \quad (12)$$

376 where  $\beta_{(r)}^A$  represents the value from the first estimate. With  
 377 several iterations of (10) and (12) (we name this iteration the  
 378 ‘‘aerosol iteration’’), we can get a stable solution for  $\beta_{(r)}^A$ , which  
 379 does not change significantly from one iteration step to the next.  
 380 The aerosol iteration stop criterion is defined as  $\xi_{(l)}^A < \xi_{min}^A$ .  
 381  $\xi_{(l)}^A$  is the relative total difference of the backscatter coefficients  
 382 between two adjacent iteration steps and is defined as

$$\xi_{(l)}^A = \frac{1}{\sum_{r=r_e}^{r_{ref}} \beta_{(r,l)}^A} \sum_{r=r_e}^{r_{ref}} \left| \beta_{(r,l)}^A - \beta_{(r,l+1)}^A \right| \quad (13)$$

383 where  $l$  represents the iteration step,  $r_e$  is the starting range  
 384 of the lidar retrieval, and  $\beta_{(r,l)}^A$  are the backscatter coefficients  
 385 at range  $r$  and iteration step  $l$ .  $\xi_{min}^A$  is typically 0.01 for our  
 386 aerosol retrievals. Aside from  $\xi_{min}^A$ , the number of iterations  
 387 required for a stable solution is also related to the range res-  
 388 olution of the signal. For simplicity, we assume that the power-  
 389 law dependences with wavelength for the aerosol extinction  
 390 and backscatter coefficients are the same although they can

be different theoretically.  $\Delta n_{(r+\Delta r)}^b$  and  $\Delta n_{(r+\Delta r)}^o$  can be  
 approximated as [39]

$$\Delta n_{(r+\Delta r)}^b \approx \frac{(4-\eta)\Delta\lambda}{2\Delta r \Delta\sigma_{O_3} \lambda_{off}} \left( \frac{B(r)}{1+B(r)} - \frac{B(r+\Delta r)}{1+B(r+\Delta r)} \right) \quad (14)$$

$$\Delta n_{(r+\Delta r)}^o \approx - \frac{\Delta\lambda}{\Delta\sigma_{O_3} \lambda_{off}} \left( \eta \alpha_{(r+\Delta r/2)}^A + 4\alpha_{(r+\Delta r/2)}^M \right) \quad (15)$$

where  $\eta$  is the Ångström exponent,  $\Delta\lambda$  is the wavelength  
 separation, and  $B(r)$  is the aerosol-to-molecular backscatter  
 ratio at the offline wavelength defined as

$$B(r) = \beta_{(r)}^A / \beta_{(r)}^M. \quad (16)$$

The estimate for the aerosol-corrected ozone number density  
 profile is then substituted into (10) to calculate an updated  
 aerosol backscatter profile, which, in turn, is used to compute  
 an updated aerosol-corrected ozone profile. This iteration is  
 named ‘‘ozone iteration’’ to be distinct with the coupled aerosol  
 iteration process. A similar iteration stop criterion,  $\xi_{(l)}^{O_3} < \xi_{min}^{O_3}$ ,  
 as the aerosol iteration, can be defined for the ozone iteration  
 by replacing the backscatter coefficient in (13) with the ozone  
 number density. Typically, only two ozone iterations are re-  
 quired when  $\xi_{min}^{O_3}$  is set equal to 0.001.

The lidar ratio ( $S$ ) exhibits a wide range of variation with  
 different aerosol refractive indexes, size distributions, and hu-  
 midity [70]. The  $S$  measurements have been made most fre-  
 quently at 308 [71] and 355 nm [72], [73]. The  $S$  for our DIAL  
 wavelengths was assumed to be 60 sr<sup>-1</sup> [74] constant over the  
 measurement range for typical urban aerosols. The Ångström  
 exponent ( $\eta$ ) is often seen as an indicator of aerosol particle  
 size. Values greater than two correspond to small smoke parti-  
 cles, and values smaller than one correspond to large particles  
 like sea salt [75], [76]. Most of the reported  $\eta$ 's for tropospheric  
 aerosol are measured at wavelengths longer than 300 nm with  
 a variation from zero to two [77], [78]. Considering that  $\eta$   
 could be relatively small when it is applied in the UV region,  
 we assume that  $\eta = 0.5$  at our DIAL wavelengths for urban  
 aerosols [79].

Simulations were conducted to investigate the aerosol cor-  
 rection in the DIAL retrieval under an extremely large aerosol  
 gradient condition by assuming the aerosol, molecular, and  
 ozone extinction profiles at 291 nm shown in Fig. 5. The  
 hypothetical aerosol profile includes the following three basic  
 regimes: homogeneous, increasing, and decreasing extinction.  
 The aerosol extinction coefficients are set equal to 10<sup>-5</sup> m<sup>-1</sup>  
 below 1.2 km and above 3 km to represent a background value.  
 The resulting steep gradient between the low background and  
 high aerosol value provides an extreme test for the aerosol cor-  
 rection algorithm. The molecular extinction profile is derived  
 from the 1976 U.S. Standard Atmosphere [80]. The assumed  
 ozone extinction profile is constant with altitude and is based on  
 a number density of 1.5 × 10<sup>12</sup> molec · cm<sup>-3</sup> and an absorption  
 cross section of 1.24 × 10<sup>-13</sup> cm<sup>2</sup> · molec<sup>-1</sup> at 291 nm [81].

Fig. 6 shows the comparison of the ozone retrieval both  
 with and without aerosol correction, as well as the calculated  
 aerosol profile, at 291 nm. This example calculation assumes  
 that  $\eta = 0.5$  and  $S = 60$  sr<sup>-1</sup> are known exactly, and there

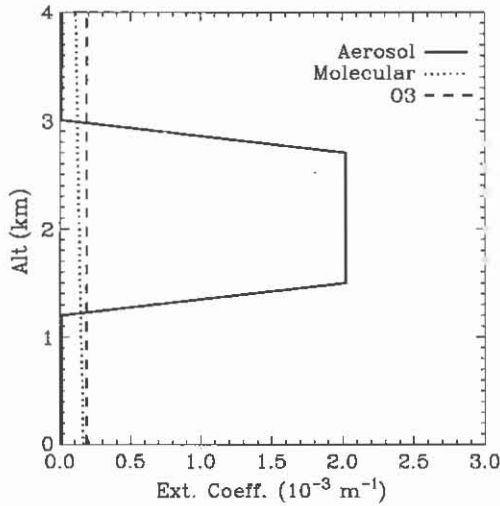


Fig. 5. Aerosol, molecular, and ozone extinction coefficient profiles at 291 nm for a model calculation of extreme aerosol effects.

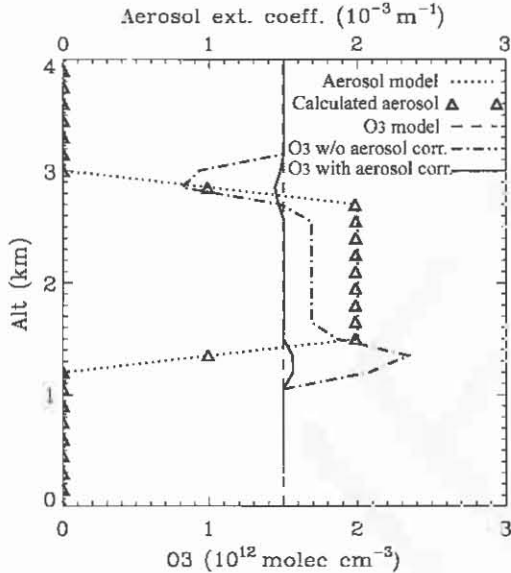


Fig. 6. Comparison of the simulated ozone retrieval without aerosol correction against that with aerosol correction using the iterative procedure. The Ångström exponent ( $\eta$ ) and lidar ratio ( $S$ ) were assumed to be exactly known at 0.5 and 60  $\text{sr}^{-1}$ , respectively, for the aerosol correction. The aerosol correction dramatically improves the ozone retrieval.

440 is no signal measurement error. With a range resolution of  
441 150 m, two ozone iterations produce the final aerosol-corrected  
442 ozone retrieval by setting  $\xi_{\min}^{\text{O}_3} = 0.001$ . In the process of cal-  
443 culating the aerosol profile, aerosol iterations produce a stable  
444 aerosol solution by setting  $\xi_{\min}^{\text{A}} = 0.01$ , which is approximately  
445 identical to the model aerosol profile. The aerosol correction  
446 procedure reduces the retrieval errors from  $\pm 50\%$  to about  
447  $\pm 5\%$ . The residual errors are due to the numerical integration  
448 and the approximation of (14) and (15). The quality of this  
449 iterative procedure depends on the choice of  $S$  and  $\eta$ . According  
450 to (10), (14) and (15),  $S$  affects the aerosol profile retrieval,  
451 while  $\eta$  affects only the final ozone correction.

452 Fig. 7 shows the sensitivity test for  $S$  and  $\eta$  in the aerosol  
453 correction assuming that  $S = 60$  and  $\eta = 0.5$  are the correct

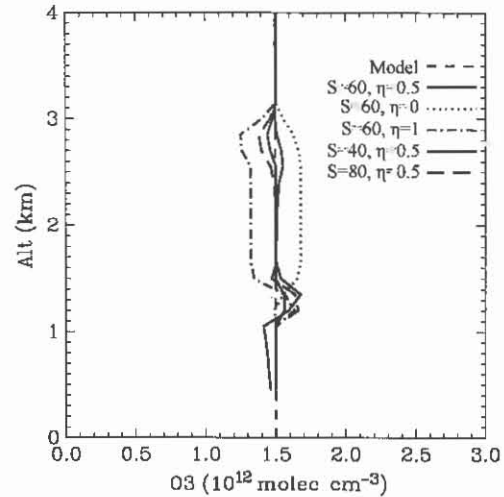


Fig. 7. Ozone retrieval using different Ångström exponents ( $\eta = 0, 0.5,$  and 1) and lidar ratios ( $S = 40, 60,$  and 80) in the aerosol correction.

454 values. Inaccurate estimates of  $S$  or  $\eta$  can yield retrieval errors  
455 up to about 20%. Larger  $\eta$  will overestimate  $\Delta n^c$ , which  
456 produces less ozone, and vice versa.  $\eta$  has a smaller impact  
457 on  $\Delta n^b$  relative to  $\Delta n^e$  due to the  $4 - \eta$  factor. The impact  
458 of  $S$  is larger in the inhomogeneous aerosol layer than in the  
459 homogeneous layer. The peak error is larger for underestimated  
460  $S$  relative to overestimated  $S$  [82].

461 We summarize the iterative procedure as follows.

- 462 1) Calculate the first estimate of the ozone concentration  
463 from (3).
- 464 2) Substitute the first estimated ozone into (10) to derive the  
465 aerosol backscatter profile for the offline wavelength, and  
466 iterate to obtain a stable solution with (12).
- 467 3) Calculate the differential aerosol backscatter and extinc-  
468 tion corrections to obtain a second estimate of ozone  
469 using (14) and (15).
- 470 4) With the second ozone estimate, go back to step 2.

#### IV. MEASUREMENTS

471

472 Fig. 8 shows an ozone DIAL retrieval for 15 consecutive  
473 hours from 12:56 local time, August 9, to 03:56, August 10,  
474 2008, with 10-min temporal integration (12 000 shots) and  
475 750-m vertical range resolution using the data processing de-  
476 scribed in the previous section. The aerosol correction was  
477 made only at altitudes between 1 and 4 km using the data  
478 from the low-altitude channel because of the negligible aerosol  
479 effects above 4 km. The aerosol time-height curtain [Fig. 8(a)]  
480 exhibits moderate aerosol activity below 2 km with expected  
481 diurnal PBL variation and shorter timescale fluctuations due to  
482 PBL processes. The maximum aerosol correction in Fig. 8(b)  
483 corresponds to an ozone adjustment of 3–4 ppbv and occurs  
484 between 1.5 and 2.5 km for the largest vertical backscatter  
485 gradient. The retrievals for the two altitude channels overlap  
486 between 3.3 and 4.4 km to produce the final ozone profiles  
487 [Fig. 8(c)] that agree well with the colocated ozonesonde (EN-  
488 SCI model 2Z with unbuffered 2% cathode solution) launched  
489 at 13:49 local time. The time-height curtain of ozone's  
490

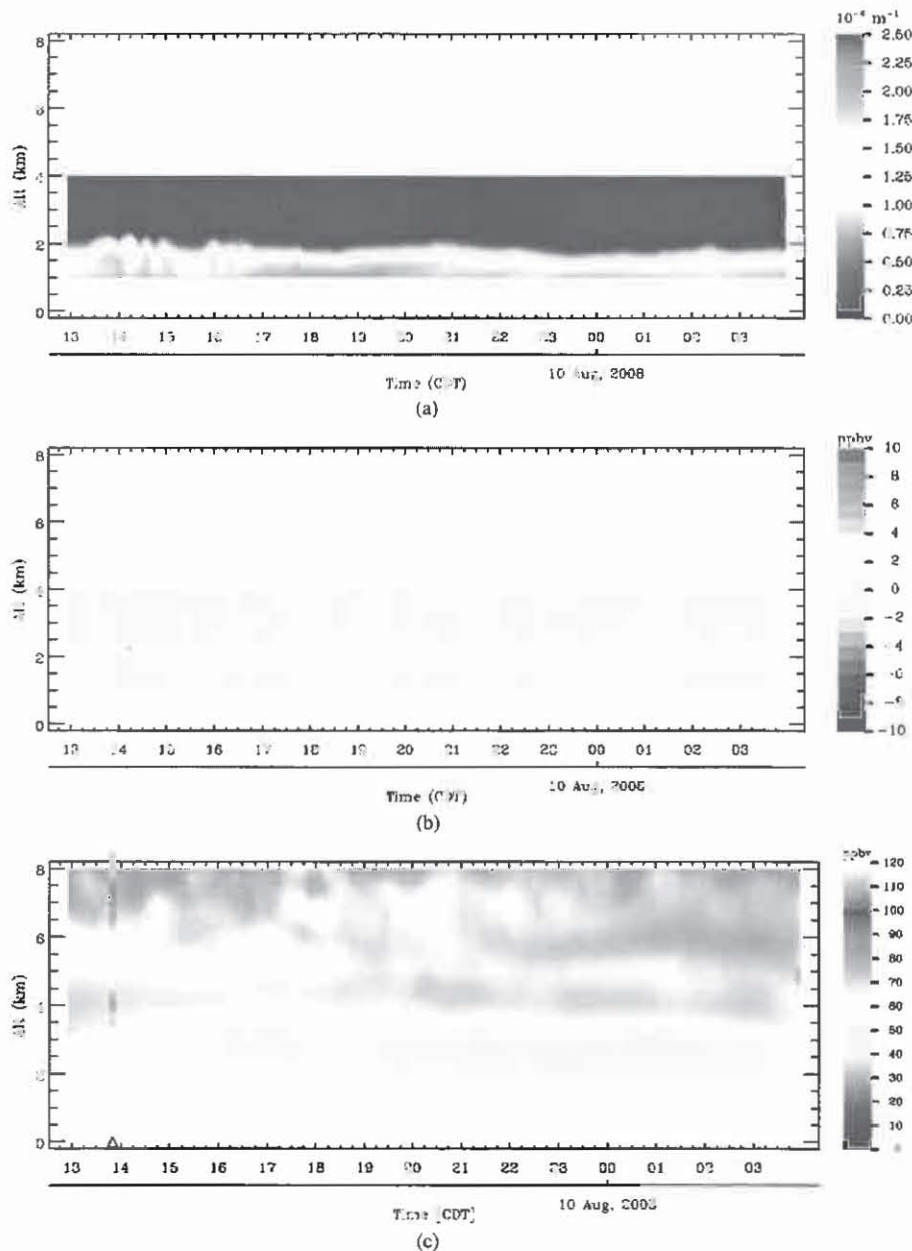


Fig. 8. Ozone DIAL retrievals made on August 9–10, 2008. (a) Calculated aerosol extinction coefficient at 291 nm. The feature at 2 km, 14:00 is a cloud. (b) Aerosol correction for ozone DIAL retrieval. (c) Ozone DIAL retrieval after aerosol correction. The retrieval was made with a 750-m vertical range resolution and a 10-min temporal resolution. The collocated ozonesonde marked by a triangle was launched at 13:49 local time.

490 evolution shows a very interesting structure of multiple ozone  
 491 layers in the lower atmosphere that varies with time. One can  
 492 see the buildup and decay of various layers throughout this  
 493 12-h period. The high-frequency variation in the high-altitude  
 494 channel ( $\geq 6$  km) results partly from lower SNR and higher  
 495 uncertainty of the SIB correction, both of which increase with  
 496 altitude. Fig. 9 shows the mean ozone profile and one-sigma  
 497 standard deviation for the 10-min vertical profiles between  
 498 12:56 and 15:06 local time in Fig. 8, as well as the coinci-  
 499 dent ozonesonde measurement. The high-altitude channel has a  
 500 standard deviation increasing with altitude due to the statistical  
 501 error distribution. Its standard deviation is less than 13 ppbv

below 8 km and increases to about 45 ppbv at 8.5 km where the  
 285-nm laser does not have sufficient SNR for ozone retrieval;  
 therefore, we terminate the retrievals at 8 km in Fig. 8. The stan-  
 dard deviation of the low-altitude channel retrievals is less than  
 5 ppbv below 4 km and reaches 8 ppbv at 5 km due to lower  
 SNR. The standard deviation at 2 km is a little larger than the  
 surrounding altitudes possibly because of larger ozone fluctu-  
 ations or larger uncertainties of the aerosol correction in the  
 ozone retrieval at the PBL top. The two altitude channels have  
 consistent mean retrievals in the overlap region with discrepan-  
 cies less than 5 ppbv and similar standard deviations at 3.3 km  
 which most likely reflect the true ozone short-term variations

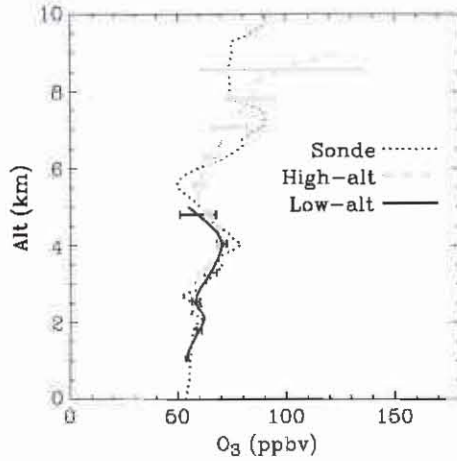


Fig. 9. Mean ozone mixing ratio and one-sigma standard deviation for the 10-min vertical profiles between 12:56 and 15:06 local time in Fig. 8. The collocated ozonesonde was launched at 13:49 local time. The large error bar ( $\sim 45\%$ ) at 8.5 km identifies the high-altitude limit of the retrievals (8 km).

514 above the PBL as shown in Fig. 8. The mean retrievals agree  
515 with the ozonesonde measurement within about 10 ppbv and  
516 have higher biases at the upper altitudes.

517

#### V. ERROR ANALYSIS

518 We divide the error budget of the DIAL retrieval into the  
519 following four categories: 1) statistical uncertainties  $\varepsilon_1$  arising  
520 from signal and background noise fluctuations; 2) errors  $\varepsilon_2$   
521 associated with differential backscatter and extinction of non-  
522 ozone gases ( $O_2$ ,  $SO_2$ ,  $NO_2$ , etc.) and aerosols; 3) errors  $\varepsilon_3$   
523 due to uncertainties in the ozone absorption cross section; and  
524 4) errors  $\varepsilon_4$  related to instrumentation and electronics.  $\varepsilon_1$  is a  
525 random error;  $\varepsilon_2$ ,  $\varepsilon_3$ , and  $\varepsilon_4$  are systematic errors.  $\varepsilon_1$  can be  
526 written as [41]

$$\varepsilon_1 = \frac{1}{2\pi\Delta r\Delta\sigma_{O_3}} \sqrt{\sum_{j,\lambda} \frac{1}{(SNR_{j,\lambda})^2}} \quad (17)$$

527 With the assumption of a Poisson distribution governing PC,  
528 the SNR at wavelength  $\lambda$  and range registration  $j$  becomes

$$SNR_{j,\lambda} = \frac{P_{j,\lambda}}{(P_{j,\lambda} + P_b + P_d)^{1/2}} \quad (18)$$

529 where  $P_b$  is the solar background counts and  $P_d$  is the dark  
530 counts. It is straightforward to show that  $\varepsilon_1$  is proportional  
531 to  $(\Delta r^3 N A P_L)^{-1/2}$ , where  $N$  represents the total number of  
532 shots,  $A$  is the unobscured area of the telescope's primary  
533 mirror, and  $P_L$  is the number of emitted laser photons.  $\Delta r$   
534 must be chosen large enough to produce an acceptably small  
535 error. Fig. 10 shows the estimated statistical errors for the  
536 high- and low-altitude channels for a 10-min integration and a  
537 750-m range resolution.  $\varepsilon_1$  is typically less than 10% below  
538 4 km for our low-altitude channel and could be 20% at 5 km.  
539 This altitude performance gives us sufficient overlap for the  
540 two altitude channels under most atmospheric conditions. In  
541 the high-altitude channel,  $\varepsilon_1$  exceeds 25% of the retrieval ozone  
542 near  $8 \pm 1$  km, where we terminate the retrieval.

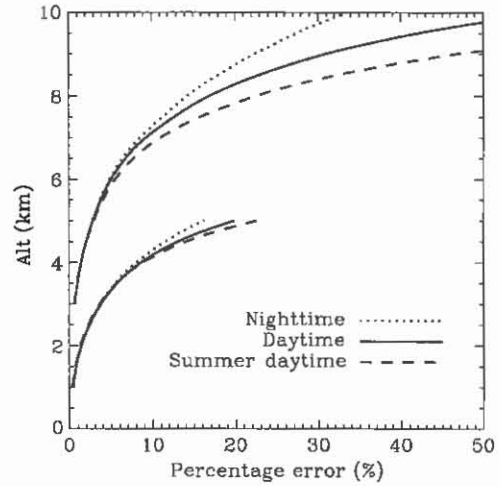


Fig. 10. Estimated statistical errors for the high- and low-altitude channels using 10-min integration and 750-m range resolution. The nighttime and daytime statistical errors are modeled by using the annually averaged local ozonesonde profile, the 1976 U.S. Standard Atmosphere, an urban aerosol model [83], and the lidar parameters in Table I. The ozone profile used for summer daytime errors is assumed 20% higher than the annual average.

$\varepsilon_2$  includes the interference from  $O_2$ ,  $SO_2$ ,  $NO_2$ , air mole-  
543 cules, and aerosols. Table II summarizes the potential errors  
544 in the DIAL retrieval for 285- and 291-nm wavelengths due  
545 to non-ozone absorption gases [84]–[88]. The calculation of  
546 the oxygen dimer ( $O_2-O_2$ ) interference includes some un-  
547 certainties due to the absorption cross-sectional measurement.  
548 The  $O_2-O_2$  absorption theory has not been entirely established  
549 [89]. Local  $SO_2$  and  $NO_2$  profiling data are not available. How-  
550 ever, the estimated error due to either  $SO_2$  or  $NO_2$  using the  
551 latest ground observation is less than 1%. The impact caused by  
552 differential Rayleigh extinction results in an inaccuracy of less  
553 than 1% using balloon ozonesonde retrievals of atmospheric  
554 density or by employing climatological models. 555

The main concern comes from the aerosol interference,  
556 which depends on both the wavelengths and wavelength sep-  
557 aration. Although the aerosol optical properties could be re-  
558 trieved from a third wavelength, the differential effect for a  
559 DIAL wavelength pair still has some uncertainty due to the  
560 assumption for lidar ratio and Ångström exponent. Within the  
561 PBL, where the statistical errors are small, differential aerosol  
562 backscattering and extinction dominate the error sources [39],  
563 [41], [43]. However, it is reasonable to believe that the error  
564 due to aerosol interference is smaller than 20% after the aerosol  
565 correction, as shown in Section III-D. 566

The uncertainty in the Bass–Paur ozone cross sections is  
567 believed to be less than 2% [81], [84], [89].  $\varepsilon_3$  will be less than  
568 3% after considering the temperature dependence. 569

$\varepsilon_4$  could be caused by a misalignment of the lasers with  
570 the telescope FOV, imperfect dead time, or SIB correction.  
571 Dead time distorts the near-range signal, and SIB distorts the  
572 far-range signal. Because the dead-time behavior is reliably  
573 characterized, the error caused by SIB usually is larger than  
574 the dead-time error. These errors related to the signal non-  
575 linearity can be experimentally diagnosed by a function-  
576 generator-driven LED laser simulator [90], [91]. For the 10-min  
577 integration data,  $\varepsilon_4$  is estimated to be  $< 5\%$  at 1–4 km for our  
578

TABLE II  
 DIAL RETRIEVAL ERRORS DUE TO NON-OZONE ABSORPTION GASES

Gases	$\Delta\sigma$ , differential absorption cross-section ( $\text{cm}^2 \text{molec}^{-1}$ ) for 285 and 291 nm	References for $\Delta\sigma$	Mixing ratio (ppbv)	References for mixing ratio	O <sub>3</sub> retrieval error (%)
O <sub>3</sub>	$1.15 \times 10^{-18}$	Bass and Paur 1981 [84]	60		
O <sub>2</sub> <sup>a</sup>	$4.5 \times 10^{-27}$	Fally et al. 2000 [85]	$2.1 \times 10^8$		1.5%
SO <sub>2</sub>	$-4.8 \times 10^{-20}$	Rufus et al. 2003 [86]	13 <sup>b</sup>	NREM 2006 [88]	-0.9%
NO <sub>2</sub>	$-2.25 \times 10^{-20}$	Bogumil et al. 2003 [87]	18 <sup>c</sup>	NREM 2006 [88]	-0.6%
Total					$\pm 1.5\%$

<sup>a</sup> due to O<sub>2</sub>-O<sub>2</sub>

<sup>b</sup> maximum 24-hr average in 1994. Latest local monitoring data available.

<sup>c</sup> Annual arithmetic average in 1993. Latest local monitoring data available.

 TABLE III  
 SUMMARY OF THE ERRORS IN RAPCD OZONE DIAL MEASUREMENTS

Errors	Low-altitude channel (1-4 km)	High-altitude channel (3-8 km)
1. $\epsilon_1$ , statistical error	<10%	<25%
2. $\epsilon_2$ , interference by non-ozone species		
Aerosol	<20%	<5%
Non-ozone absorption gases		<1.5%
Rayleigh	<1% using local radiosonde profile	
3. $\epsilon_3$ , due to uncertainty in $\Delta\sigma_{\text{O}_3}$		<3%
4. $\epsilon_4$ , due to SIB and dead-time	<5%	<10%
Total RMS error	<23%	<28%

\* The errors are estimated by assuming a 60 ppbv constant ozone mixing ratio in the troposphere for data with a 750-m vertical resolution and 10-min integration.

579 low-altitude channel and < 10% for our high-altitude channel  
 580 below 8 km based on our LED test results and the analysis of  
 581 our previous data such as Figs. 8 and 9. A summary of the errors  
 582 in the DIAL measurements is shown in Table III for a constant  
 583 tropospheric ozone of 60 ppbv, 750-m vertical resolution, and  
 584 10-min integration.

585 Fig. 11 shows a comparison of 12 lidar retrievals and their  
 586 single coincident ozonesonde measurement between 13:00 and  
 587 14:00 local time except for the first profile on August 17, 2008  
 588 (upper right panel), which was taken at 08:00. The aerosol  
 589 correction was made at altitudes between 1 and 4 km by setting  
 590 the reference altitude at  $\sim 6$  km and  $\beta_{(\text{ref})}^{\lambda} = 1.67 \times 10^{-7} \text{ m}^{-1} \cdot$   
 591  $\text{sr}^{-1}$  [83]. Fig. 12 shows the mean percentage differences and  
 592 their standard errors of the mean for all those retrievals. The li-  
 593 dar retrievals of the low-altitude channel agree with ozonesonde  
 594 measurements within 10% from 1 to 4 km. The relatively  
 595 high errors at about 2 km possibly relate to residual aerosol  
 596 correction errors around PBL height. The lidar retrievals from  
 597 the high-altitude channel agree with ozonesonde to within 20%  
 598 below 8 km. The statistical error and the uncertainty associated

with the SIB correction result in larger errors for the high- 599  
 altitude channel above 6 km. 600

## VI. CONCLUSION AND FUTURE PLANS

601

The RAPCD ozone DIAL system measures tropospheric 602  
 ozone profiles during both daytime and nighttime using the 603  
 285-/291-nm wavelength pair. The low-altitude receiving chan- 604  
 nel makes ozone measurements at altitudes between 1 and 5 km 605  
 using a 10-cm telescope and Hamamatsu R7400U PMTs. The 606  
 high-altitude channel measures ozone between 3 and about 607  
 8 km using a 40-cm telescope and EMI 9813 PMTs. Model 608  
 calculations demonstrate that the iterative aerosol correction 609  
 procedure significantly reduces the retrieval error arising from 610  
 differential aerosol backscatter in the lower troposphere where 611  
 the quality of the aerosol correction depends on the accuracy of 612  
 the *a priori* lidar ratio and Ångström exponent. A comparison 613  
 of the lidar retrievals and coincident ozonesonde measurements 614  
 suggests that retrieval accuracy ranges from better than 10% 615  
 after the application of an aerosol correction below 4 km to 616

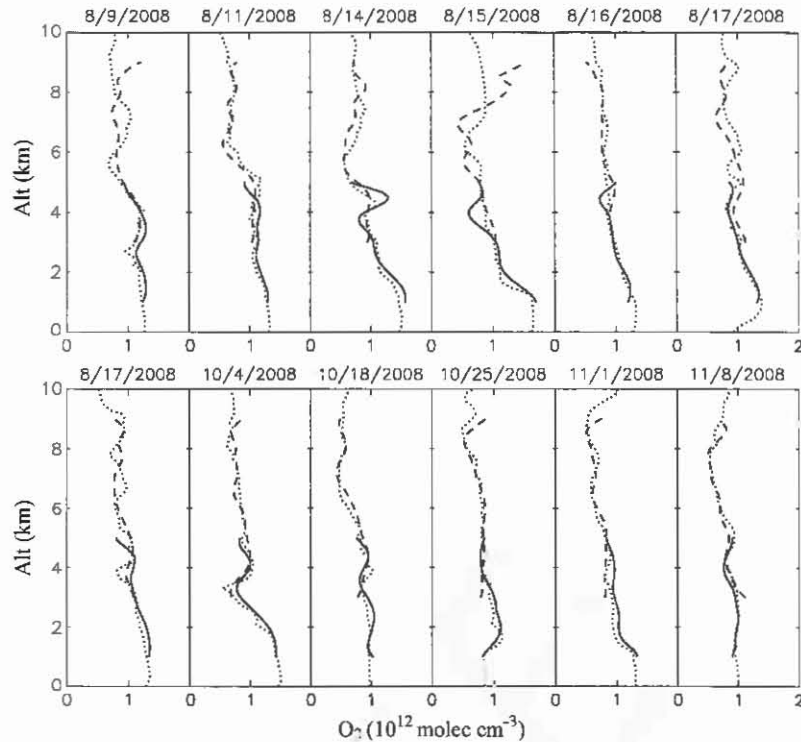


Fig. 11. Comparison of the (solid) low- and (dashed) high-altitude-channel aerosol-corrected retrievals with the (dotted) coincident ozonesonde measurements.

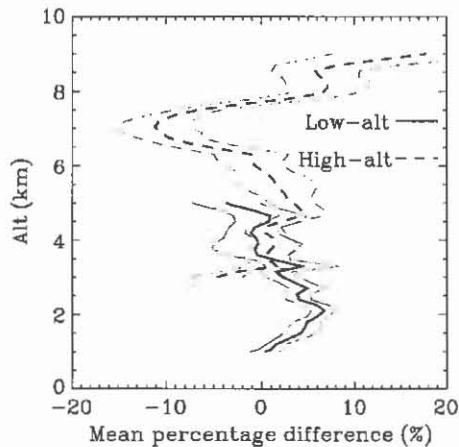


Fig. 12. (Dark) Mean percentage differences, lidar sonde/sonde, and (gray) their estimated one-sigma standard error of the mean for the data in Fig. 11.

617 better than 20% for altitudes below 8 km with 750-m vertical  
618 resolution and 10-min integration. Error sources include sta-  
619 tistical uncertainty, differential scattering and absorption from  
620 non-ozone species, uncertainty in ozone absorption cross sec-  
621 tion, and imperfection of the dead-time and SIB corrections.  
622 The uncertainty in the SIB correction and the statistical errors  
623 dominate the error sources in the free troposphere and could be  
624 reduced by increasing the integration time or reducing the range  
625 resolution.

626 Future improvements will overcome two major limitations  
627 of the current system by doing the following: 1) extending  
628 observations into the upper troposphere by replacing the current  
629 transmitters with more powerful ones and shifting the current

wavelengths to longer ones to make higher-altitude nighttime  
630 measurements and 2) minimizing aerosol interference in the  
631 lower troposphere by adding a third wavelength (dual-DIAL  
632 technique). This lidar with expected improvements will provide  
633 a unique data set to investigate the chemical and dynamical  
634 processes in the PBL and free troposphere. The spatiotemporal  
635 variance estimates derived from the ozone lidar observations  
636 will also be useful for assessing the variance of tropospheric  
637 ozone captured by satellite retrievals. 638

#### ACKNOWLEDGMENT

The authors would like to thank T. McGee, S. McDermid,  
640 and T. Leblanc for the extensive discussions, J. Kaye,  
641 P. K. Bhartia, and R. McPeters for the continuing support,  
642 and the UAHuntsville ozonesonde team, namely, R. Williams,  
643 P. Buckley, and D. Nuding, for providing the ozonesonde data.  
644 The authors would also like to thank W. Guerin for editing the  
645 manuscript. 646

#### REFERENCES

- [1] D. Jacob, *Introduction to Atmospheric Chemistry*. Princeton, NJ: Prince- 648  
ton Univ. Press, 1999, pp. 199–200. 649
- [2] D. Shindell, G. Faluvegi, A. Lacis, J. Hansen, R. Ruedy, and E. Aguilar, 650  
“Role of tropospheric ozone increases in 20th-century climate change,” 651  
*J. Geophys. Res.*, vol. 111, no. D8, p. D08 302, Apr. 2006. 652
- [3] J. Lelieveld and F. J. Dentener, “What controls tropospheric ozone?,” 653  
*J. Geophys. Res.*, vol. 105, no. D3, pp. 3531–3551, Feb. 2000. 654
- [4] J. Stutz, B. Alicke, R. Ackermann, A. Geyer, A. White, and E. Williams, 655  
“Vertical profiles of NO<sub>3</sub>, N<sub>2</sub>O<sub>5</sub>, O<sub>3</sub>, and NO<sub>x</sub> in the nocturnal bound- 656  
ary layer: 1. Observations during the Texas Air Quality Study 2000,” 657  
*J. Geophys. Res.*, vol. 109, no. D12, p. D12 306, Jun. 2004. 658

659 [5] A. Geyer and J. Stutz, "Vertical profiles of NO<sub>3</sub>, N<sub>2</sub>O<sub>5</sub>, O<sub>3</sub>, and NO<sub>x</sub> in  
660 the nocturnal boundary layer: 2. Model studies on the altitude dependence  
661 of composition and chemistry," *J. Geophys. Res.*, vol. 109, no. D12,  
662 p. D12 307, Jun. 2004.

663 [6] J. Liang, L. W. Horowitz, D. J. Jacob, Y. Wang, A. M. Fiore, J. A. Logan,  
664 G. M. Gardner, and J. W. Munger, "Seasonal budgets of reactive nitrogen  
665 species and ozone over the United States, and export fluxes to the global  
666 atmosphere," *J. Geophys. Res.*, vol. 103, no. D11, pp. 13435–13450,  
667 Jun. 1998.

668 [7] W. B. Grant, E. V. Browell, C. F. Butler, M. A. Fenn, M. B. Clyton,  
669 J. R. Hannan, H. E. Fuelberg, D. R. Blake, N. J. Blake, G. L. Gregory,  
670 B. G. Heikes, G. W. Sachse, H. B. Singh, J. Snow, and R. W. Talbot,  
671 "A case study of transport of tropical marine boundary layer and lower  
672 tropospheric air masses to the northern midlatitude upper troposphere,"  
673 *J. Geophys. Res.*, vol. 105, no. D3, pp. 3757–3769, Feb. 2000.

674 [8] H. Eisele, H. E. Scheel, R. Sladkovic, and T. Trickl, "High-resolution lidar  
675 measurements of stratosphere–troposphere exchange," *J. Atmos. Sci.*,  
676 vol. 56, no. 2, pp. 319–330, Jan. 1999.

677 [9] A. Stohl, P. Bonasoni, P. Cristofanelli, W. Collins, J. Feichter, A. Frank,  
678 C. Forster, E. Gerasopoulos, H. Gäggler, P. James, T. Kentarchos,  
679 H. Kromp-Kolb, B. Krüger, C. Land, J. Meloen, A. Papayannis,  
680 A. Priller, P. Seibert, M. Sprenger, G. J. Roelofs, H. E. Scheel,  
681 C. Schnabel, P. Siegmund, L. Tobler, T. Trickl, H. Wernli, V. Wirth,  
682 P. Zanis, and C. Zerefos, "Stratosphere–troposphere exchange: A review  
683 and what we learned from STACCATO," *J. Geophys. Res.*, vol. 108,  
684 no. D12, p. 8516, 2003.

685 [10] A. O. Langford, C. D. Masters, M. H. Proffitt, E.-Y. Hsie, and A. F. Tuck,  
686 "Ozone measurements in a tropopause fold associated with a cut-off low  
687 system," *Geophys. Res. Lett.*, vol. 23, no. 18, pp. 2501–2504, 1996.

688 [11] A. J. DeCaria, K. E. Pickering, G. L. Stenchikov, and L. E. Ott,  
689 "Lightning-generated NO<sub>x</sub> and its impact on tropospheric ozone production:  
690 A three-dimensional modeling study of a stratosphere–troposphere  
691 experiment: Radiation, aerosols and ozone (STRAO-A) thunderstorm,"  
692 *J. Geophys. Res.*, vol. 110, no. D14, p. D14 303, Jul. 2005.

693 [12] O. R. Cooper, A. Stohl, M. Trainer, A. M. Thompson, J. C. Witte,  
694 S. J. Oltmans, G. Morris, K. E. Pickering, J. H. Crawford, G. Chen,  
695 R. C. Cohen, T. H. Bertram, P. Wooldridge, A. Perring, W. H. Brune,  
696 J. Merrill, J. L. Moody, D. Tarasick, P. Nédélec, G. Forbes,  
697 M. J. Newchurch, F. J. Schmidlin, B. J. Johnson, S. Turquet,  
698 S. L. Baughcum, X. Ren, F. C. Fehsenfeld, J. F. Meagher, N. Spichtinger,  
699 C. C. Brown, S. A. McKeen, I. S. McDermid, and T. Leblanc, "Large  
700 upper tropospheric ozone enhancements above midlatitude North America  
701 during summer: *In situ* evidence from the IONS and MOZARC ozone  
702 measurement network," *J. Geophys. Res.*, vol. 111, no. D24, p. D24 S05,  
703 Dec. 2006.

704 [13] O. R. Cooper, M. Trainer, A. M. Thompson, S. J. Oltmans, D. W. Tarasick,  
705 J. C. Witte, A. Stohl, S. Eckhardt, J. Lelieveld, M. J. Newchurch,  
706 B. J. Johnson, R. W. Portmann, L. Kalnajs, M. K. Dubej, T. Leblanc,  
707 I. S. McDermid, G. Forbes, D. Wolfe, T. Carey-Smith, G. A. Morris,  
708 B. Lefebvre, B. Rappenglück, E. Joseph, F. Schmidlin, J. Meagher,  
709 F. C. Fehsenfeld, T. J. Keating, R. A. V. Curen, and K. Minschwaner,  
710 "Evidence for a recurring eastern North America upper tropospheric  
711 ozone maximum during summer," *J. Geophys. Res.*, vol. 112, no. D23,  
712 p. D23 304, Dec. 2007.

713 [14] U. Schumann and H. Huntrieser, "The global lightning-induced nitrogen  
714 oxides source," *Atmos. Chem. Phys.*, vol. 7, no. 14, pp. 3823–3907,  
715 2007.

716 [15] S. J. Oltmans, H. Levy, II, J. M. Harris, J. T. Merrill, J. L. Moody,  
717 J. A. Lathrop, E. Cuevas, M. Trainer, M. S. O'Neill, J. M. Prospero,  
718 H. Vömel, and B. J. Johnson, "Summer and spring ozone profiles over  
719 the North Atlantic from ozonesonde measurements," *J. Geophys. Res.*,  
720 vol. 101, no. D22, pp. 29 179–29 200, Dec. 1996.

721 [16] M. J. Newchurch, M. A. Ayoub, S. Oltmans, B. Johnson, and  
722 F. J. Schmidlin, "Vertical distribution of ozone at four sites in the United  
723 States," *J. Geophys. Res.*, vol. 108, no. D1, p. 4031, Jan. 15, 2003.

724 [17] R. D. McPeters, G. J. Labow, and B. J. Johnson, "A satellite-derived  
725 ozone climatology for balloonsonde estimation of total column ozone,"  
726 *J. Geophys. Res.*, vol. 102, no. D7, pp. 8875–8885, Apr. 1997.

727 [18] J. P. Burrows, M. Weber, M. Buchwitz, V. Rozanov,  
728 A. Ladstätter-Weienmayer, A. Richter, R. DeBeek, R. Hoogen,  
729 K. Bramstedt, K.-U. Eichmann, and M. Eisinger, "The Global Ozone  
730 Monitoring Experiment (GOME): Mission concept and first scientific  
731 results," *J. Atmos. Sci.*, vol. 56, no. 2, pp. 151–175, Jan. 1999.

732 [19] M. J. Newchurch, D. M. Cunnold, and J. Cao, "Intercomparison of  
733 Stratospheric Aerosol and Gas Experiment (SAGE) with Umkehr[64] and  
734 Umkehr[92] ozone profiles and time series: 1979–1991," *J. Geophys.  
735 Res.*, vol. 103, no. D23, pp. 31 277–31 292, Dec. 1998.

[20] M. J. Newchurch, E. S. Yang, D. M. Cunnold, G. C. Reinsel,  
736 J. M. Zawodny, and J. M. Russell, III, "Evidence for slowdown in 737  
738 stratospheric ozone loss: First stage of ozone recovery," *J. Geophys. Res.*,  
739 vol. 108, no. D16, p. 4507, Aug. 23, 2003.

[21] J. M. Russell, III, L. L. Gordley, J. H. Park, S. R. Drayson, W. D. Heaketh,  
740 R. J. Cicerone, A. F. Tuck, J. E. Frederick, J. E. Harries, and P. J. Crutzen,  
741 "The halogen occultation experiment," *J. Geophys. Res.*, vol. 98, no. D6,  
742 p. 10 777–10 797, Jun. 1993.

[22] J. W. Waters, L. Froidevaux, G. L. Manney, W. G. Read, and L. S. Elson,  
743 "MLS observations of lower stratospheric ClO and O<sub>3</sub> in the 1992 south-  
744 ern hemisphere winter," *Geophys. Res. Lett.*, vol. 20, no. 12, pp. 1219–  
745 1222, Jun. 1993.

[23] X. Liu, K. Chance, C. E. Sioris, R. J. D. Spurr, T. P. Kurosu, R. V. Martin,  
746 "Ozone profile and tropospheric ozone retrievals  
747 from global ozone monitoring experiment: Algorithm description and  
748 validation," *J. Geophys. Res.*, vol. 110, no. D20, p. D20 307, Oct. 2005.

[24] J. R. Ziemke, S. Chandra, B. N. Duncan, L. Froidevaux, P. K. Bhartia,  
749 P. F. Levelt, and J. W. Waters, "Tropospheric ozone determined from Aura  
750 OMI and MLS: Evaluation of measurements and comparison with the  
751 global modeling initiative's chemical transport model," *J. Geophys. Res.*,  
752 vol. 111, no. D19, p. D19 303, Oct. 2006.

[25] Y. Choi, Y. Wang, T. Zeng, D. Cunnold, E.-S. Yang, R. Martin, K. Chance,  
753 V. Thouet, and E. Edgerton, "Springtime transitions of NO<sub>2</sub>, CO, and O<sub>3</sub>  
754 over North America: Model evaluation and analysis," *J. Geophys. Res.*,  
755 vol. 113, no. D20, p. D20 311, Oct. 2008.

[26] Q. Yang, D. M. Cunnold, H.-J. Wang, L. Froidevaux, H. Claude,  
756 J. Merrill, M. Newchurch, and S. J. Oltmans, "Midlatitude tropospheric  
757 ozone columns derived from the Aura Ozone monitoring instrument and  
758 microwave limb sounder measurements," *J. Geophys. Res.*, vol. 112,  
759 no. D20, p. D20 305, Oct. 2007, DOI:10.1029/2007JD008528.

[27] J. H. Kim, M. J. Newchurch, and K. Han, "Distribution of tropical tropo-  
760 spheric ozone determined by the scan-angle method applied to TOMS  
761 measurements," *J. Atmos. Sci.*, vol. 58, no. 18, pp. 2699–2708, Sep. 2001.

[28] J. H. Kim and M. J. Newchurch, "Biomass-burning influence on tropo-  
762 spheric ozone over New Guinea and South America," *J. Geophys. Res.*,  
763 vol. 103, no. D1, pp. 1455–1461, Jan. 1998.

[29] J. H. Kim, S. Na, M. J. Newchurch, and R. V. Martin, "Tropical tropo-  
764 spheric ozone morphology and seasonality seen in satellite and *in situ*  
765 measurements and model calculations," *J. Geophys. Res.*, vol. 110,  
766 no. D2, p. D02 303, Jan. 2005.

[30] X. Liu, K. Chance, C. E. Sioris, T. P. Kurosu, R. Spurr, R. V. Martin, T. Fu,  
767 J. Logan, D. Jacob, P. Palmer, M. J. Newchurch, I. A. Megretskaia, and  
768 R. B. Chatfield, "First directly retrieved global distribution of tropospheric  
769 column ozone from GOME: Comparison with the GEOS-CHEM model,"  
770 *J. Geophys. Res.*, vol. 111, no. D2, p. D02 308, Jan. 2006.

[31] X. Liu, K. Chance, C. E. Sioris, T. P. Kurosu, and M. J. Newchurch,  
771 "Intercomparison of GOME, ozonesonde, and SAGE II measurements of  
772 ozone: Demonstration of the need to homogenize available ozonesonde  
773 data sets," *J. Geophys. Res.*, vol. 111, no. D14 305, Jul. 2006.

[32] R. Beer, "TES on the Aura mission: Scientific objectives, measurements,  
774 and analysis overview," *IEEE Trans. Geosci. Remote Sens.*, vol. 44, no. 5,  
775 pp. 1102–1105, May 2006.

[33] P. F. Levelt, E. Hilsenrath, G. W. Leppelmeier, G. H. J. van den Oord,  
776 P. K. Bhartia, J. Tamminen, J. F. de Haan, and J. P. Veeckind, "Science  
777 objectives of the ozone monitoring instrument," *IEEE Trans. Geosci.  
778 Remote Sens.*, vol. 44, no. 5, pp. 1199–1208, May 2006.

[34] W. Steinbrecht, T. J. McGee, L. W. Twigg, H. Claude, F. Schönenborn,  
779 G. K. Sunnicht, and D. Silbert, "Intercomparison of stratospheric ozone  
780 and temperature profiles during the October 2005 Hohenpeißenberg  
781 Ozone Profiling Experiment (HOPE)," *Atmos. Meas. Tech.*, vol. 2, no. 1,  
782 pp. 125–145, 2009.

[35] T. Trickl, N. Bärtsch-Ritter, H. Eisele, M. Furger, R. Mücke, and A. Stohl,  
783 "High-ozone layers in the middle and upper troposphere above Central  
784 Europe: Strong import from the stratosphere over the Pacific Ocean,"  
785 *Atmos. Chem. Phys. Discuss.*, vol. 9, no. 1, pp. 3113–3166, Jan. 2009.

[36] Y. Zhao, R. D. Marchbanks, and R. M. Hardesty, "ETL's transportable  
786 lower troposphere ozone lidar and its applications in air quality studies,"  
787 *Proc. SPIE*, vol. 3127, pp. 53–62, 1997.

[37] R. J. Alvarez, II, W. A. Brewer, D. C. Law, J. L. Machol,  
788 R. D. Marchbanks, S. P. Sandberg, C. J. Senff, and A. M. Weickmann,  
789 "Development and application of the TOPAZ airborne lidar system by  
790 the NOAA Earth System Research Laboratory," in *Proc. 24th Int. Laser  
791 Radar Conf.*, 2008, pp. 68–71.

[38] G. Ancellet, A. Papayannis, J. Pelon, and G. Mégie, "DIAL tropospheric  
792 ozone measurement using a Nd:YAG laser and the Raman shifting  
793 technique," *J. Atmos. Oceanic Technol.*, vol. 6, no. 5, pp. 832–839,  
794 Oct. 1989.

- 813 [39] E. V. Browell, S. Ismail, and S. T. Shipley, "Ultraviolet DIAL measurements of O<sub>3</sub> profiles in regions of spatially inhomogeneous aerosols," *Appl. Opt.*, vol. 24, no. 17, pp. 2827–2836, Sep. 1985.
- 816 [40] T. Fukuchi, T. Fujii, N. Cao, and K. Nemoto, "Tropospheric O<sub>3</sub> measurements by simultaneous differential absorption lidar and null profiling," *Opt. Eng.*, vol. 40, no. 9, pp. 1944–1949, Sep. 2001.
- 817 [41] A. Papayannis, G. Ancellet, J. Pelon, and G. Mégie, "Multiwavelength lidar for ozone measurements in the troposphere and the lower stratosphere," *Appl. Opt.*, vol. 29, no. 4, pp. 467–476, Feb. 1990.
- 822 [42] M. H. Proffitt and A. O. Langford, "Ground-based differential absorption lidar system for day or night measurements of ozone throughout the free troposphere," *Appl. Opt.*, vol. 36, no. 12, pp. 2568–2585, Apr. 1997.
- 826 [43] J. A. Sunesson, A. Apituley, and D. P. J. Swart, "Differential absorption lidar system for routine monitoring of tropospheric ozone," *Appl. Opt.*, vol. 33, no. 30, pp. 7045–7058, Oct. 1994.
- 829 [44] J. L. Machol, R. D. Marchbanks, C. J. Senff, B. J. McCarty, W. L. Eberhard, W. A. Brewer, R. A. Richter, R. J. Alvarez, II, D. C. Law, A. M. Weickmann, and S. P. Sandberg, "Scanning tropospheric ozone and aerosol lidar with double-gated photomultipliers," *Appl. Opt.*, vol. 48, no. 3, pp. 512–524, Jan. 2009.
- 834 [45] I. S. McDermid, D. A. Haner, M. M. Kleiman, T. D. Walsh, and M. L. White, "Differential absorption lidar system for tropospheric and stratospheric ozone measurements," *Opt. Eng.*, vol. 30, no. 1, pp. 22–30, Jan. 1991.
- 838 [46] T. J. McGee, M. R. Gross, U. N. Singh, J. J. Butler, and P. E. Kimvilakani, "Improved stratospheric ozone lidar," *Opt. Eng.*, vol. 34, no. 5, pp. 1421–1430, May 1995.
- 841 [47] J. Pelon, S. Godin, and G. Mégie, "Upper stratospheric (30–50 km) lidar observations of the ozone vertical distribution," *J. Geophys. Res.*, vol. 91, no. D8, pp. 8667–8671, 1986.
- 844 [48] O. Uchino and I. Tabata, "Mobile lidar for simultaneous measurements of ozone, aerosols, and temperature in the stratosphere," *Appl. Opt.*, vol. 30, no. 15, pp. 2005–2012, May 1991.
- 847 [49] E. V. Browell, S. Ismail, and W. B. Grant, "Differential absorption lidar (DIAL) measurements from air and space," *Appl. Phys. B, Photophys. Laser Chem.*, vol. 67, no. 4, pp. 399–410, Oct. 1998.
- 850 [50] O. R. Cooper, A. Stohl, S. Eckhardt, D. D. Parrish, S. J. Oltmans, B. J. Johnson, P. Nédélec, F. J. Schmidlin, M. J. Newchurch, Y. Kondo, and K. Kita, "A springtime comparison of tropospheric ozone and transport pathways on the east and west coasts of the United States," *J. Geophys. Res.*, vol. 110, no. D5, p. D05 S90, Mar. 2005.
- 855 [51] G. J. Megie, G. Ancellet, and J. Pelon, "Lidar measurements of ozone vertical profiles," *Appl. Opt.*, vol. 24, no. 21, pp. 3454–3463, Nov. 1985.
- 857 [52] A. E. Siegman, Standard for the Measurement of Beam Widths, Beam Divergence, and Propagation Factors. Proposal for a Working Draft ISO1991.
- 860 [53] J. Burris, W. Heaps, B. Gary, W. Hoegy, L. Lait, T. McGee, M. Gross, and U. Singh, "Lidar temperature measurements during the Tropical Ozone Transport Experiment (TOTE)/Vortex Ozone Transport Experiment (VOTE) mission," *J. Geophys. Res.*, vol. 103, no. D3, pp. 3505–3510, 1998.
- 865 [54] J. Burris, T. McGee, W. Hoegy, P. Newman, L. Lait, L. Twigg, G. Sumnicht, W. Heaps, C. Hostetler, R. Neuber, and K. F. Künzi, "Lidar temperature measurements during the SOLVE campaign and the absence of polar stratospheric clouds from regions of very cold air," *J. Geophys. Res.*, vol. 107, no. D20, p. 8297, Oct. 2002.
- 870 [55] D. P. Donovan, J. A. Whiteway, and A. I. Carswell, "Correction for nonlinear photon-counting effects in lidar systems," *Appl. Opt.*, vol. 32, no. 33, pp. 6742–6753, Nov. 1993.
- 873 [56] M. Lampton and J. Bixler, "Counting efficiency of systems having both paralyzable and nonparalyzable elements," *Rev. Sci. Instrum.*, vol. 56, no. 1, pp. 164–165, Jan. 1985.
- 876 [57] D. N. Whiteman, B. Demoz, P. D. Girolamo, J. Comer, I. Veselovskii, K. Evans, Z. Wang, M. Cadirola, K. Rush, G. Schwemmer, B. Gentry, S. H. Melfi, B. Mielke, D. Venable, and T. V. Hove, "Raman lidar measurements during the International H<sub>2</sub>O Project. Part I: Instrumentation and analysis techniques," *J. Atmos. Ocean. Technol.*, vol. 23, no. 2, pp. 157–169, Feb. 2006.
- 882 [58] R. K. Newsom, D. D. Turner, B. Mielke, M. Clayton, R. Ferrare, and C. Sivaraman, "Simultaneous analog and photon counting detection for Raman lidar," *Appl. Opt.*, vol. 48, no. 20, pp. 3903–3914, Jul. 2009.
- 885 [59] Photomultiplier Handbook, Burle, Lancaster, PA, 1989.
- 886 [60] F. Cairo, F. Congeduti, M. Poli, S. Centurioni, and G. D. Donfrancesco, "A survey of the signal-induced noise in photomultiplier detection of wide dynamics luminous signals," *Rev. Sci. Instrum.*, vol. 67, no. 9, pp. 3274–3280, Sep. 1996.
- [61] Y. Zhao, "Signal-induced fluorescence in photomultipliers in differential absorption lidar systems," *Appl. Opt.*, vol. 38, no. 21, pp. 4639–4648, 891 Jul. 1999.
- [62] T. J. McGee, R. A. Ferrare, D. N. Whiteman, J. J. Butler, J. F. Burris, and M. A. Owens, "Lidar measurements of stratospheric ozone during the STOIC campaign," *J. Geophys. Res.*, vol. 100, no. D5, pp. 9255–9262, 895 1995.
- [63] M. R. Measures, *Laser remote sensing: Fundamentals and applications*. 897 New York: Wiley, 1984.
- [64] V. A. Kovalev and W. E. Eichinger, *Elastic Lidar Theory, Practice, and Analysis Methods*. New York: Wiley, 2004.
- [65] J. R. Taylor, *An Introduction to Error Analysis: The Study of Uncertainties in Physical Measurements*. Mill Valley, CA: Oxford Univ. Press, 902 1982.
- [66] F. Immler, "A new algorithm for simultaneous ozone and aerosol retrieval from tropospheric DIAL measurements," *Appl. Phys. B, Photophys. Laser Chem.*, vol. 76, no. 5, pp. 593–596, May 2003.
- [67] Y. Sasano, "Simultaneous determination of aerosol and gas distribution by DIAL measurements," *Appl. Opt.*, vol. 27, no. 13, pp. 2640–2641, 908 Jul. 1988.
- [68] V. A. Kovalev and M. P. Bristow, "Compensational three-wavelength differential-absorption lidar technique for reducing the influence of differential scattering on ozone-concentration measurements," *Appl. Opt.*, vol. 35, no. 24, pp. 4790–4797, Aug. 1996.
- [69] Z. Wang, H. Nakane, H. Hu, and J. Zhou, "Three-wavelength dual differential absorption lidar method for stratospheric ozone measurements in the presence of volcanic aerosols," *Appl. Opt.*, vol. 36, no. 6, pp. 1245–1252, Feb. 1997.
- [70] R. Pedros, V. Estelles, M. Sicard, J. L. Gomez-Amo, M. P. Utrillas, J. A. Martinez-Lozano, F. Rocadenbosch, C. Perez, and J. M. B. Recio, "Climatology of the aerosol extinction-to-backscatter ratio from sun-photometric measurements," *IEEE Trans. Geosci. Remote Sens.*, vol. 48, no. 1, pp. 237–249, Jan. 2010.
- [71] A. Ansmann, M. Riebesell, U. Wandinger, C. Weitkamp, W. E. Voss, W. Lahmann, and W. Michaelis, "Combined Raman elastic-backscatter LIDAR for vertical profiling of moisture, aerosol extinction, backscatter, and LIDAR ratio," *Appl. Phys. B, Photophys. Laser Chem.*, vol. 55, no. 1, pp. 18–28, Jul. 1992.
- [72] R. Ferrare, S. Melfi, D. Whiteman, K. Evans, and R. Leifer, "Raman lidar measurements of aerosol extinction and backscattering 1. Methods and comparisons," *J. Geophys. Res.*, vol. 103, no. D16, pp. 19 663–19 672, 930 1998.
- [73] D. Müller, A. Ansmann, I. Mattis, M. Tesche, U. Wandinger, D. Althausen, and G. Pisani, "Aerosol-type-dependent lidar ratios observed with Raman lidar," *J. Geophys. Res.*, vol. 112, no. D16, p. D16 202, Aug. 934 2007.
- [74] J. Ackermann, "The extinction-to-backscatter ratio of tropospheric aerosol: A numerical study," *J. Atmos. Ocean. Technol.*, vol. 15, no. 4, pp. 1043–1050, Aug. 1998.
- [75] D. Westphal and O. Toon, "Simulations of microphysical, radiative, and dynamical processes in a continental scale forest fire smoke plume," *J. Geophys. Res.*, vol. 96, no. D12, pp. 22 379–22 400, 941 1991.
- [76] G. L. Schuster, O. Dubovik, and B. N. Holben, "Ångström exponent and bimodal aerosol size distributions," *J. Geophys. Res.*, vol. 111, no. D7, pp. D07 207 1–D07 207 14, Apr. 2006.
- [77] C. M. Carrico, M. H. Bergin, J. Xu, K. Baumann, and H. Maring, "Urban aerosol radiative properties: Measurements during the 1999 Atlanta Supersite experiment," *J. Geophys. Res.*, vol. 108, no. D7, p. 8-422, 947 Feb. 2003.
- [78] D. Müller, I. Mattis, U. Wandinger, A. Ansmann, D. Althausen, and A. Stohl, "Raman lidar observations of aged Siberian and Canadian forest fire smoke in the free troposphere over Germany in 2003: Microphysical particle characterization," *J. Geophys. Res.*, vol. 110, no. D17, p. D17 201, 952 Sep. 2005.
- [79] T. F. Eck, B. N. Holben, J. S. Reid, O. Dubovik, A. Smirnov, N. T. O'Neill, I. Slutsker, and S. Kinne, "Wavelength dependence of the optical depth of biomass burning, urban, and desert dust aerosols," *J. Geophys. Res.*, vol. 104, no. D24, pp. 31 333–31 349, Dec. 27, 1999.
- [80] NOAA. U.S. Standard Atmosphere, Washington, DC: Government Printing Office, 1976.
- [81] J. Orphal and K. Chance, "Ultraviolet and visible absorption cross-sections for HITRAN," *J. Quant. Spectrosc. Radiat. Transf.*, vol. 82, no. 1–4, pp. 491–504, Nov./Dec. 2003.
- [82] V. A. Kovalev, "Sensitivity of the lidar solution to errors of the aerosol backscatter-to-extinction ratio: Influence of a monotonic change in the aerosol extinction coefficient," *Appl. Opt.*, vol. 34, no. 18, pp. 3457–3462, 965 Jun. 1995.

967 [83] A. S. Jursa, *Handbook of Geophysics and the Space Environment*.  
 968 Hanscom AFB, MA: Air Force Geophys. Lab., 1985.  
 969 [84] A. M. Bass and R. J. Paur, "Absorption cross-sections for ozone: The  
 970 temperature dependence," *J. Photochem.*, vol. 17, p. 141, 1981.  
 971 [85] S. Fally, A. C. Vandaele, M. Carleer, C. Hermans, A. Jenouvrier,  
 972 M.-F. Mérienne, B. Coquart, and R. Colin, "Fourier transform spec-  
 973 troscopy of the O<sub>2</sub> Herzberg bands. III. Absorption cross-sections of  
 974 the collision-induced bands and of the Herzberg continuum," *J. Mol.*  
 975 *Spectrosc.*, vol. 204, no. 1, pp. 10–20, Nov. 2000.  
 976 [86] J. Rufus, G. Stark, P. L. Smith, J. C. Pickering, and A. P. Thorne, "High-  
 977 resolution photoabsorption cross section measurements of SO<sub>2</sub>, 2: 220 to  
 978 325 nm at 295 K," *J. Geophys. Res.*, vol. 108, no. E2, p. 5011, Feb. 2003.  
 979 [87] K. Bogumil, J. Orphal, T. Homann, S. Voigt, P. Spietz, O. C. Fleischmann,  
 980 A. Vogel, M. Hartmann, H. Bovensmann, J. Frerick, and J. P. Burrows,  
 981 "Measurements of molecular absorption spectra with the SCIAMACHY  
 982 pre-flight model: Instrument characterization and reference data for at-  
 983 mospheric remote-sensing in the 230–2380 nm region," *J. Photochem.*  
 984 *Photobiol. A, Chem.*, vol. 157, no. 2/3, pp. 167–184, May 2003.  
 985 [88] Air Quality Report, Data Summaries, Trend Analysis and Program  
 986 Activities (2001–2005), Natural Resources Environ. Manage. Division,  
 987 Huntsville, AL, 2006.  
 988 [89] J. Orphal, "A critical review of the absorption cross-sections of O<sub>3</sub> and  
 989 NO<sub>2</sub> in the 240–790 nm region," *J. Photochem. Photobiol. A*, vol. 157,  
 990 no. 2/3, pp. 185–209, May 2003.  
 991 [90] M. P. Bristow, D. H. Bundy, and A. G. Wright, "Signal linearity, gain  
 992 stability, and gating in photomultipliers: Application to differential ab-  
 993 sorption lidars," *Appl. Opt.*, vol. 34, no. 21, pp. 4437–4452, Jul. 1995.  
 994 [91] H. S. Lee, G. K. Schwemmer, C. L. Corb, M. Dombrowski, and  
 995 C. Prasad, "Gated photomultiplier response characterization for DIAL  
 996 measurements," *Appl. Opt.*, vol. 29, no. 22, pp. 3303–3315, Aug. 1, 1990.

997  
 998  
 999  
 1000  
 1001  
 1002  
 1003  
 1004  
 1005



**Shi Kuang** received the M.Sc. degree in electrical engineering and the Ph.D. degree in atmospheric science from The University of Alabama in Huntsville (UAHuntsville), Huntsville, in 2009.  
 He is currently with the Earth System Science Center, Atmospheric Science Department, UAHuntsville. His current fields of interest include lidar remote sensing, tropospheric ozone, and air quality study.

1006  
 1007  
 1008  
 1009  
 1010  
 1011  
 1012  
 1013  
 1014



**John F. Burris** received the Ph.D. degree in physics from the University of Maryland, College Park.  
 He is currently a Lidar Scientist with the Goddard Space Flight Center, National Aeronautics and Space Administration, Greenbelt, MD, where he has been employed for 30 years. The focus of his work involves developing lidar systems to measure ozone, temperature, CO<sub>2</sub>, and CH<sub>4</sub> remotely on Earth and Mars.



**Michael J. Newchurch** received the B.Sc. degree in industrial sciences from Colorado State University, Fort Collins, in 1974 and the Ph.D. degree in atmospheric sciences from the Georgia Institute of Technology, Atlanta, in 1986.  
 Since 1988, he has been with the Atmospheric Science Department, The University of Alabama in Huntsville (UAHuntsville), Huntsville, where he is currently a Professor. He conceived, designed, built, and currently directs the Regional Atmospheric Profiling Center for Discovery laboratory and the UAHuntsville/National Oceanic and Atmospheric Administration Ozone sonde station. His current fields of interest include tropospheric ozone profile measurements with lidars and ozonesondes, retrievals from satellite instruments, atmospheric photochemical modeling, and ozone trend analyses.

1015  
 1016  
 1017  
 1018  
 1019  
 1020  
 1021  
 1022  
 1023  
 1024  
 1025  
 1026  
 1027  
 1028  
 1029



**Steve Johnson** received the B.S.E.E. degree from Purdue University, West Lafayette, IN, in 1977 and the M.S.E.E. degree from The University of Alabama in Huntsville, Huntsville, in 1987.  
 He is currently with the Earth Science Office, Marshall Space Flight Center, National Aeronautics and Space Administration, Huntsville, where he has worked in the development and application of lidars and radiometers for profiling of winds and atmospheric constituents.

1030  
 1031  
 1032  
 1033  
 1034  
 1035  
 1036  
 1037  
 1038  
 1039



**Stephanie Long** received the B.Sc. degree in physics from The University of Alabama in Huntsville (UAHuntsville), Huntsville, in 2010.  
 Since 2007, she has been with the Atmospheric Chemistry Group, National Space Science and Technology Center, Huntsville. Her responsibilities include the Huntsville Differential Absorption Lidar system, as well as managing the Huntsville Ozonesonde Station.

1040  
 1041  
 1042  
 1043  
 1044  
 1045  
 1046  
 1047  
 1048  
 1049  
 1050